THE ASTROPHYSICAL JOURNAL, 488:760–775, 1997 October 20

LYMAN-ALPHA ABSORPTION AND THE D/H RATIO IN THE LOCAL INTERSTELLAR MEDIUM[1]

ANDREW R. DRING,[2] J. LINSKY,[3] JAYANT MURTHY,[2] R. C. HENRY,[2] W. MOOS,[2]
A. VIDAL-MADJAR,[4] J. AUDOUZE,[4] AND W. LANDSMAN[5]
Received 1997 March 10; accepted 1997 May 28

ABSTRACT

Using the Goddard High Resolution Spectrograph onboard the *Hubble Space Telescope*, we have observed Lyα absorption against stellar chromospheres along six lines of sight, with additional observations of the Mg II H and K lines along five of the lines of sight and Fe II absorption along four of the lines of sight. We found absorption near the projected velocity of the local interstellar cloud (LIC) along three lines of sight. The velocity toward the stars β Gem and σ Gem was only marginally consistent with the LIC. The single interstellar component toward 31 Com had a velocity that was inconsistent with the projected LIC velocity. Three of the lines of sight showed a multicomponent velocity structure. For the star ϵ Eri we required an additional hot, low-density component which we have interpreted as a stellar hydrogen wall. The LIC temperatures derived from our data range from 7800 to 9700 K with values of the microturbulence parameter less than 2.0 km s^{-1}. The measured D/H ratio for the LIC along every sight line is consistent with a value of 1.6×10^{-5}, the best determined value being the β Cas line of sight with $D/H = 1.7 \pm 0.3 \times 10^{-5}$.

Subject headings: ISM: abundances — ISM: bubbles — ISM: clouds — ISM: kinematics and dynamics — ultraviolet: ISM

1. INTRODUCTION

Recent observations have enabled a detailed study of the local interstellar medium (LISM). The main features thus far observed are that the Sun is embedded at the edge of a warm Galactic cloud which is itself embedded in a hot, low-density region termed the local bubble (Frisch & York 1983). The local Bubble extends roughly 60 pc in most directions but reaches almost 300 pc in the direction $l = 235°$ and $b = -14°$ (Welsh 1991; Welsh et al. 1994). The hot Local Bubble is believed to be carved out of the denser ISM either by OB associations or by supernova explosions (Cox & Reynolds 1987). The warm cloud in which the Sun is embedded, termed the local interstellar cloud (LIC), extends a few parsecs in some directions (Linsky, Piskunov, & Wood 1996) but has several smaller clouds around it. The LIC moves with a velocity 25.7 km s^{-1} in the direction of $l = 186.°1$ and $b = -16.°4$ (Lallement & Bertin 1992) and has an average density of 0.1 H cm^{-3} and a temperature of 7000 K (Linsky et al. 1995).

Very often an additional hot, low-density component is needed to fit the observed H I profile. Bertin et al. (1995) interpreted the hot component toward Sirius A as a layer of heated gas at the cloud/hot interstellar medium (HISM) interface. Models of the conductive interface between the warm and hot ISM (see, e.g., Borkowski, Balbus, & Fristrom 1990; Dalton & Balbus 1993) predict absorption from highly ionized species such as C IV, Si IV, AND N V, but Bertin et al. (1995) failed to detect significant C IV absorption towards Sirius A. Gry et al. (1995) do claim to have observed C IV absorption towards ϵ CMa and use it as evidence for a conductive front. Linsky & Wood (1996) and Wood, Alexander, & Linsky (1996) have interpreted these hot components as hydrogen walls formed either at the solar heliopause due to the motion of the heliosphere through the LIC or an analogous cloud wall around the observed star. Star hydrogen walls are predicted by models of the solar/stellar wind interaction (e.g., Baranov & Malama 1995). Both interpretations of the hot, low-density components need to be considered more closely. We do find an additional hot, low-density component towards ϵ Eri which we interpret as a stellar hydrogen wall surrounding the star (see § 6).

One parameter of primary importance to cosmological theories is the D/H ratio because it is a sensitive indicator of the total baryonic density of the universe. For an $\Omega_b h_{50}^2 = 1.0$ universe the primordial D/H ratio is 10^{-9}, and for an $\Omega_b h_{50}^2 = 0.1$ universe it is a few $\times 10^{-5}$ (Schramm 1993). Since there are no effective means of creating deuterium (Epstein, Lattimer, & Schramm 1976) and since deuterium is easily destroyed in stars, the D/H ratio observed today must be lower then the primordial value, and therefore an absolute lower limit (upper limit) on the D/H ratio (baryon density). There have been many measurements of the D/H ratio by looking at deuterated molecules in sea water (Boato 1954a), meteorites (Boato 1954b), Jupiter (Gautier & Owens 1989), and in comets (Balsiger, Altwegg, & Geiss 1995), but all of these methods give values that are too high due to fractionation effects (Geiss & Reeves 1981). Some observations have been made of Lyα absorption in quasars at high redshifts (Carswell et al. 1996; Rugers & Hogan 1996; Tytler, Fan, & Burles 1996; Tytler, Burles, & Kirkman 1997, in preparation), which potentially has the advantage of detecting the D/H ratio closer to the promordial value. While the first two groups argue in favor of a

[1] Based on observations with the NASA/ESA *Hubble Space Telescope*, obtained at the Space Telescope Science Institute, which is operated by the Association of Universities for Research in Astronomy, Inc., under NASA contract NAS 5-26555.

[2] Department of Physics and Astronomy, Johns Hopkins University, Baltimore, MD 21218.

[3] Joint Institute for Laboratory Astrophysics, University of Colorado and National Institute for Standards and Technology, Boulder, CO 80309-0440.

[4] Centre Nationale de Recherche Spatiale Institut d'Astrophysique, 98 bis Boulevard Arago, F-75014 Paris, France.

[5] Hughes STX, Inc., Code 681, Goddard Space Flight Center, Greenbelt, MD 20771.

TABLE 1

OBSERVED STARS

HD	Name	Spectral Type	l (deg)	b (deg)	V_{LIC} (km s^{-1})	Distance (pc)
432.....	β Cas	F2 II	117.52	−3.27	9.4	13.9
11443	α Tri	F6 IV	138.64	−31.40	18.0	17.5
22049	ϵ Eri	K2 V	195.86	−48.04	21.6	3.3
62044	σ Gem	K1 III	191.19	23.27	19.7	55.5
62509	β Gem	K0 II	192.23	23.41	19.6	10.6
111812.....	31 Com	G0 II	114.93	89.58	−7.2	90.9

high primordial D/H $\sim$ 2–3 $\times$ 10^{-4}, Tytler and collaborators argue quite convincingly that the primordial D/H is significantly lower, e.g., $\sim$2–4 $\times$ 10^{-5}. The discussion is not yet settled on this very important point (Songaila, Wampler, & Cowie 1997). Because astration makes is difficult to compare local measurements with measurements made at high redshifts, it is important to obtain precise determinations of D/H in both regimes.

2. OBSERVATIONS

We have obtained seven sets of Goddard High Resolution Spectrograph (GHRS) (see Soderblom et al. 1993 for a review of GHRS) observations of six stars during the months of 1995 August–September. The stars are spectral types F, G, and K and are located within 100 pc of the Sun. One star, σ Gem, is a binary and was observed twice, once on September 5 at orbital phase 0.697 and once on September 15 at orbital phase 0.158, with the phases derived from Eker (1985). The stars are listed in Table 1 along with spectral type, galactic latitude and longitude, and distance in parsecs.

All seven observations contain echelle A spectra of the Lyα region from 1211–1218 Å. These spectra were taken with the large science aperture of the GHRS and have a spectral resolution of $\lambda/\delta\lambda = 84000$, with signal to noise (S/N) ranging from 100–200. The observations starting times and exposure duration for these spectra are listed in Table 2. Also listed in Table 2 are spectra taken with the echelle B grating of the region 2593–2605 Å containing the Fe II λ2600 line and the region 2792–2807 Å containing the Mg II H and K lines. These spectra were also taken with the large science aperture and have a resolution of

TABLE 2

OBSERVATIONS SUMMARY FOR PROPOSAL 5879

Grating and Order	Aperture and Substep Pattern	Wavelength Range (Å)	Exposure Time (s)	Observation Start Time (UT hr:min)
		β Cas (1995 Aug 7)		
Echelle A-46	LSA 7	1211–1218	8268	03:56
Echelle B-22	LSA 7	2593–2605	326	02:43
Echelle B-20	LSA 7	2792–2807	326	02:51
		α Tri (1995 Aug 23)		
Echelle A-46	LSA 7	1211–1218	4787	20:05
Echelle B-22	LSA 7	2593–2605	326	18:29
Echelle B-20	LSA 7	2792–2807	326	18:37
		ϵ Eri (1995 Aug 8)		
Echelle A-46	LSA 7	1211–1218	7398	23:04
Echelle B-22	LSA 7	2593–2605	326	22:03
		σ Gem (1995 Sep 5); orbital phase 0.697		
Echelle A-46	LSA 7	1211–1218	4787	23:37
Echelle B-20	LSA 7	2792–2807	109	22:42
		σ Gem (1995 Sep 14); orbital phase 0.158		
Echelle A-46	LSA 7	1211–1218	4787	00:51
Echelle B-20	LSA 7	2792–2807	109	23:59
		β Gem (1995 Sep 26)		
Echelle A-46	LSA 7	1211–1218	7834	00:52
Echelle B-20	LSA 7	2792–2807	326	23:51
		31 Com (1995 Aug 8)		
Echelle A-46	LSA 7	1211–1218	7398	02:49
Echelle B-22	LSA 7	2593–2605	326	01:12
		31 Com (1994 Jul 11) Archival Data: Z2DC0108T-Proposal 5323		
Echelle B-20	SSA 7	2792–2807	1293	19:10

$\lambda/\delta\lambda = 84000$. As Table 2 shows, we have Fe II data for four of the seven observations and Mg II data for six of the seven observations. All spectra were obtained in FP-SPLIT mode.

3. PROCESSING

All the spectra were run through CALHRS, the standard calibration software which includes a conversion to raw count rates, a diode response and paired pulse correction, removal of photocathode nonuniformities and vignetting, smoothing and removal of the background, an incidence angle correction and an echelle ripple correction, and finally a conversion to absolute flux and heliocentric wavelengths. The spectra, consisting of many short exposures, were then coadded using the IRAF POFFSETS and SPECALIGN procedures. Visual inspection of both the individual FP-SPLIT spectra and the final co-added spectrum revealed improper co-addition of the weaker Fe II lines, resulting in broader or multiple lines. These were co-added manually to ensure proper alignment of the individual spectra. The saturated line core had some positive flux due to instrumentally scattered light which needed to be subtracted. Following Spitzer & Fitzpatrick (1993), we averaged the flux level in the line core and subtracted that value from the entire spectra. We then removed the geocoronal Lyα line, which in every case was entirely within the line core. Finally, we converted the echelle B wavelengths from vacuum to air.

There were no specific WAVECAL observations taken that could be used to calibrate the wavelength scale, but there were SPYBAL observations taken prior to each observation. The SPYBALs were used to compute offsets for the wavelength data of all observations, and in addition we used the known position of the geocoronal emission line to calibrate the Lyα region. Despite these improvements to the wavelength scale, it should be remembered that the data were taken with the large science aperture and may be uncertain by as much as ± 2 km s^{-1}. To characterize the uncertainty in velocity measurements, we computed the standard deviation of the independent D I, Mg II, and Fe II velocity measurements for each cloud. Typically the standard deviation was ~ 1.5 km s^{-1}, so we adopted this value for our systematic uncertainty which is included in the uncertainties listed in Table 3.

4. FITTING PROCEDURE

We obtained line strengths and positions for all our lines from Morton (1991). The H and D Lyα lines are actually doublets separated by 1.33 km s^{-1} which are included in our fits. To fit the echelle B data (Fe II and Mg II lines) in most spectra we first fit the local background with a polynomial, and then fit the interstellar absorption lines with a Voigt profile. For each line there were three free parameters, the line center, v_c in km s^{-1}, the column density N in H cm^{-2}, and the line width parameter b in km s^{-1}. The profile, including the absorption lines and continuum was then convolved with the instrumental line spread function (LSF) reported by Gilliland (1994) to be nearly Gaussian with a FWHM of 4.4 pixels for post COSTAR spectra taken with the large science aperture. From the model Profile a χ^2 statistic was computed and minimized using multiparameter χ^2 minimization algorithms from Bevington (1969). Each line-fitting figure shows the observed flux, the best-fit model profile convolved with the instrument LSF, and the fit residuals along the bottom. The Lyα region figures additionally show the assumed model emission line used to fit the data.

To fit the Lyα region we developed profiles by starting with a quadratic emission then adding a stellar emission profile. We attempted several techniques to model the stellar emission line, including Gaussian line profiles, solar line profiles from Brekke et al. (1991), and observed Mg II profiles using the same $\Delta\lambda$ scale as the Lyα line (Linsky et al. 1995; Linsky & Wood 1996). In each case the best results were obtained using a two-component Gaussian profile, one broad component to fit the wings and a narrow component to fit the core region. In order to reduce the number of free parameters we fixed the H I and D I lines to have the same radial velocity and we set $b_{\rm H\,I}$ to be $(2)^{1/2} b_{\rm D\,I}$. These assumptions are valid for a well-mixed cloud where the broadening is dominated by the thermal broadening, indicated by the low values of the microturbulence parameter we derived. The emission lines of cool stars typically show self-reversals, so in each case we allowed for a self-reversal to be present in the emission line but found them necessary only along four lines of sight. No adjustment to the emission-line profiles were made other than to alter the line parameters, therefore, in some cases where the Gaussian profiles are not quite adequate, the fits show slight systematic errors. Both the H I and D I absorption lines were modeled as Voigt functions and added to the profile, and in those cases where the Mg II H and K lines or Fe II lines showed two components, we used two components for the H I and D I lines. Again the profile was convolved with the instrumental LSF and adjusted to give the lowest χ^2 fit.

After finding a best-fit model for each of our spectra, we then proceeded to estimate the uncertainties for our fit parameters. In general, the parameters are not independent

TABLE 3

INTERSTELLAR MEDIUM PARAMETERS

Star	$V_{\rm LIC}$[a] (km s^{-1})	$V_{\rm obs}$ (km s^{-1})	Temperature (10^3 K)	ξ (km s^{-1})	log ($N_{\rm H\,I}$)	D/H (10^{-5})	D(Mg)	D/Mg II	D(Fe)
β Cas	9.4	9.1 ± 1.8	9.7 ± 0.9	<1.3	18.13 ± 0.05	1.7 ± 0.3	-1.29 ± 0.08	8.4 ± 1.6	-1.29 ± 0.1
α Tri	...	13.1 ± 1.9	8.3 ± 2.0	<1.3	17.99 ± 0.10	1.0 ± 0.6	-0.83 ± 0.14	1.7 ± 0.5	-1.21 ± 0.2
	18.0	17.7 ± 1.9	8.4 ± 2.0	<1.4	18.06 ± 0.10	1.6 ± 0.6	-1.46 ± 0.14	11.8 ± 3.9	-1.17 ± 0.2
ϵ Eri	21.6	20.9 ± 1.8	7.8 ± 0.8	1.4 ± 0.4	17.88 ± 0.07	1.4 ± 0.4	...	...	-1.03 ± 0.1
σ Gem	19.7	21.5 ± 1.8	8.9 ± 1.5	1.6 ± 0.3	18.00 ± 0.10	1.4 ± 0.4	-1.07 ± 0.1	4.3 ± 1.1	...
	...	32.0 ± 1.8	7.3 ± 1.3	<1.2	17.77 ± 0.10	1.3 ± 0.4	-1.30 ± 0.1	6.9 ± 1.5	...
β Gem	19.6	22.0 ± 1.8	8.9 ± 1.5	1.9 ± 0.3	18.06 ± 0.10	1.4 ± 0.4	-1.12 ± 0.1	4.7 ± 1.1	...
	...	33.2 ± 1.8	7.3 ± 1.3	1.0 ± 0.5	17.83 ± 0.10	1.6 ± 0.4	-1.27 ± 0.1	7.6 ± 1.5	...
31 Com.....	-7.2	-3.1 ± 1.8	8.7 ± 1.0	<1.0	17.88 ± 0.06	2.0 ± 0.4	-0.97 ± 0.07	4.9 ± 0.6	-0.84 ± 0.1

[a] Local interstellar cloud velocities derived from Lallement & Bertin 1992.

since different sets of parameters can lead to equally good fits. The parameters $N_{\rm H\,I}$ and b for both the H I absorption and emission are all highly interdependent. We used the error estimation scheme described in Lampton, Margon, & Bowyer (1976). For each parameter of interest we stepped through a range of values centered on the best-fit value, fixing the parameter at each step, then reoptimizing all other free parameters to obtain a new lowest χ^2 value. We then determined the parameter values where the χ^2 statistic increased by the value χ^2_n at the 2 σ level, where n is the number of free parameters used in the fit. These parameter values were then used to define the 2 σ uncertainty range. This technique therefore includes uncertainties due to the unknown stellar emission line since the emission-line shape is allowed to vary considerably when reoptimizing the fit.

There are many systematic errors which can affect the results which we discuss here. We assume that D I and H I have the same velocities and that the line width is dominated by thermal broadening. Relaxing these assumptions for single-component lines of sight did not result in significantly different fit parameters, so we conclude that these assumptions introduce negligible errors. Of much greater concern is the possible presence of unknown components which can greatly affect the derived parameters. It is difficult to quantify how additional components may change the fits since adding additional components often makes the problem ill-defined, resulting in large uncertainties in the fits. We have taken the position throughout of using the fewest possible free parameters to fit the data. Another potential source of error is the assumption that the Mg II and Fe II lines are good tracers of the H I and D I lines. This assumption fails in the case of hot, low-density components where the Mg II and Fe II column densities are too low to be observed and may also fail if the Mg II and Fe II lines are associated with H II rather than H I regions.

5. FITTING RESULTS

The fit parameters with their random errors are listed in Table 4, and the computed temperature, microturbulence ξ, D/H ratio, and gas depletions are shown in Table 3. Some of the interesting features are discussed.

5.1. β Cas

The Fe II line and Mg II lines for β Cas, shown in Figures 1 and 2, show only one component, with velocities matching well with the projected LIC velocity. The fit for the Lyα region is shown in Figure 3. Our fit parameters can be compared with the parameters given by Piskunov et al. (1997), who analyzed a lower resolution G140M spectra of the Lyα line of β Cas. They find $b_{\rm H\,I} = 11.0 \pm 2.0$ and $\log (N_{\rm H\,I}) = 18.18 \pm 0.13$, while we find $b_{\rm H\,I} = 12.67 \pm 0.6$ and $\log (N_{\rm H\,I}) = 18.13 \pm 0.05$, which are consistent within the stated errors. It is encouraging that independent analysis of the same lines of sight do in fact yield consistent results.

5.2. α Tri

The Fe II and Mg II lines for α Tri, shown in Figures 4 and 5, are very broad and slightly asymmetric, with the Fe II line showing a resolved second component. An acceptable fit was obtained for the Lyα region with single components, but the $b_{\rm D\,I}$ value was also very broad. In addition, the single-component fits for the Mg II lines were not exceptionally good and were considerably improved with the addition of a second, unresolved, component separated by about 5 km s^{-1}. It is difficult to know whether one is dealing with distinct velocity components or observing material flowing with a small range of velocities along the line of sight, when the lines are so well blended. We have simply modeled the absorption features with two distinct components.

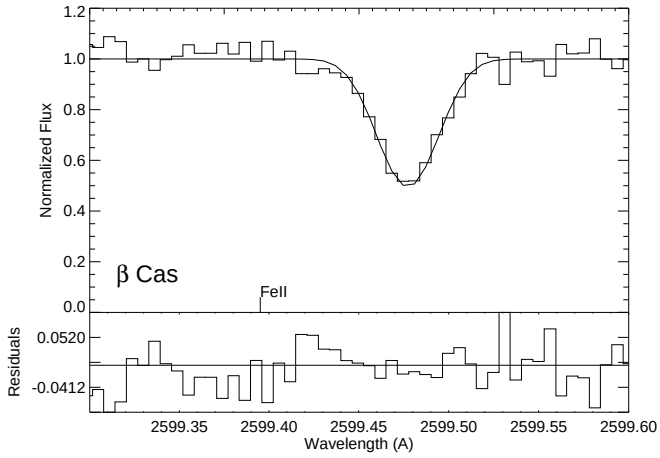

FIG. 1.—Fe II λ2599 region of β Cas showing the observed spectra, the best-fit model after convolution, and the residuals of the best fit. The continuum is normalized to unity, and the rest wavelength for Fe II is shown by the labeled tick mark.

Since the Mg II lines required two components to produce acceptable fits, we also used two components to fit the Lyα region. Unfortunately, since the absorption features were already fitted well with a single, albeit broad, component, the introduction of a second component made the fitting procedure unstable. In order to remove degrees of freedom from the fitting procedure, we fixed the velocity separation between the two components. This led to an excellent model fit in which the D/H ratios for the two components were $2.0 \pm 0.6 \times 10^{-5}$ and $0.8 \pm 0.6 \times 10^{-5}$. This fit is shown in the top half of Figure 6. While neither of the best-fit D/H ratios agrees well with other measurements of the LIC, it was apparent that equally acceptable fits could be obtained with a wide variety of D I and H I column densities. We then fixed the D/H ratio of the line which was associated with the LIC at 1.6×10^{-5}, consistent with other determinations (Piskunov et al. 1996) and found a perfectly acceptable fit, which is shown in the bottom half of Figure 6. In both fits the total hydrogen and deuterium column densities remained constant and produced a D/H ratio of 1.3×10^{-5}. The χ^2 for the second plot is almost exactly equal to that of the first, so we adopt it as our final fit since it has more physically reasonable parameters, with the caveat that a truly wide range of parameters will produce acceptable fits for α Tri.

5.3. ϵ Eri

We have no Mg II data for ϵ Eri, and our fit to the Fe II region is shown in Figure 7. The Fe II line requires only a single component and suggests single-component fits for the Lyα region. The first attempt at fitting the absorption features with no constraints on velocity or line width led to a H I line that was too broad for the D I line and blueshifted by 6 km s^{-1}. When the lines were fixed to have the same velocity and widths appropriate to a single, well-mixed, isothermal cloud, no acceptable fit was found. In order to produce a physically reasonable fit with an acceptable χ^2 we

TABLE 4

FIT PARAMETERS

Line	Velocity (km s^{-1})	b (km s^{-1})	log N	χ^2_ν
		β Cas (HD 432)		
H I.....	8.3 ± 0.3	12.67 ± 0.6	18.132 ± 0.05	0.45
D I.....	8.3 ± 0.3	8.96 ± 0.4	13.361 ± 0.06	0.45
Mg II λ2795.....	9.6 ± 0.3	2.48 ± 0.4	12.38 ± 0.06	1.11
Mg II 2802	10.1 ± 0.3	2.61 ± 0.3	12.49 ± 0.07	1.74
Fe II λ2599.....	9.5 ± 0.3	1.78 ± 0.8	12.36 ± 0.1	0.70
		α Tri (HD 11443)		
H I.....	12.5 ± 0.7	11.95 ± 1.4	17.991 ± 0.1	0.48
	16.9 ± 0.7	11.81 ± 1.4	18.062 ± 0.1	0.48
D I.....	12.5 ± 0.7	8.45 ± 1.0	12.979 ± 0.1	0.48
	16.9 ± 0.7	8.35 ± 1.0	13.266 ± 0.1	0.48
Mg II λ2795.....	14.0 ± 0.4	4.12 ± 1.4	12.73 ± 0.1	3.00
	18.7 ± 0.4	0.62 ± 1.4	12.17 ± 0.1	3.00
Mg II λ2802.....	14.4 ± 0.4	4.01 ± 1.4	12.78 ± 0.1	5.23
	18.1 ± 0.4	0.97 ± 1.4	12.23 ± 0.1	5.23
Fe II λ2599.....	12.7 ± 0.5	1.17 ± 1.0	12.29 ± 0.2	1.40
	17.6 ± 0.5	1.52 ± 1.0	12.40 ± 0.2	1.40
		ε Eri (HD 22049)		
H I.....	20.5 ± 0.7	11.44 ± 0.6	17.875 ± 0.07	0.50
D I.....	20.5 ± 0.7	8.09 ± 0.4	13.027 ± 0.06	0.50
Fe II λ2599.....	21.3 ± 0.3	2.54 ± 0.7	12.36 ± 0.07	7.56
		σ Gem (HD 62044)		
H I.....	21.4 ± 1.0	12.37 ± 1.0	17.995 ± 0.1	1.47
	32.0 ± 1.0	10.98 ± 1.0	17.767 ± 0.1	1.47
D I.....	21.4 ± 1.0	8.75 ± 0.7	13.148 ± 0.1	1.47
	32.0 ± 1.0	7.76 ± 0.7	12.893 ± 0.1	1.47
Mg II λ2795.....	21.6 ± 0.3	3.54 ± 0.3	12.50 ± 0.04	1.49
	32.0 ± 0.3	2.22 ± 0.3	12.05 ± 0.04	1.49
Mg II λ2802.....	22.0 ± 0.3	3.37 ± 0.4	12.53 ± 0.03	2.61
	32.5 ± 0.3	2.12 ± 0.4	12.07 ± 0.04	2.61
		β Gem (HD 62059)		
H I.....	21.9 ± 1.0	12.33 ± 1.0	18.059 ± 0.1	0.40
	33.0 ± 1.0	11.02 ± 1.0	17.834 ± 0.1	0.40
D I.....	21.9 ± 1.0	8.72 ± 0.7	13.201 ± 0.1	0.40
	33.0 ± 1.0	7.79 ± 0.7	13.034 ± 0.1	0.40
Mg II λ2795.....	21.7 ± 0.3	3.48 ± 0.3	12.54 ± 0.04	1.65
	32.9 ± 0.3	2.61 ± 0.3	12.14 ± 0.04	1.65
Mg II λ2802.....	22.6 ± 0.3	2.87 ± 0.5	12.51 ± 0.07	1.36
	33.8 ± 0.3	2.36 ± 0.3	12.16 ± 0.04	1.36
		31 Com (HD 111812)		
H I.....	−3.3 ± 0.6	11.96 ± 0.7	17.884 ± 0.06	0.84
D I.....	−3.3 ± 0.6	8.46 ± 0.5	13.191 ± 0.05	0.84
Mg II λ2795.....	−3.6 ± 0.3	2.41 ± 0.2	12.50 ± 0.05	2.76
Mg II λ2802.....	−2.9 ± 0.3	2.31 ± 0.1	12.50 ± 0.03	2.97
Fe II λ2599.....	−2.4 ± 0.3	0.71 ± 0.4	12.55 ± 0.1	1.16

had to introduce an additional hot, low-density component with parameters $b_{\rm H\,I} = 20$–23 km s^{-1}, log $N = 14.3$, and $v_c = 2.3$–15.0 km s^{-1}. This fit is shown in Figure 8. Notice that a very wide range of velocities can be obtained by altering the line width. Since the hot line is at the blue edge of the saturated line core, it can be shifted redward, into the line core, if it is made broader at the same time. This trade-off is characteristic of hot, low-density components where only half of the line is effectively observed. We discuss the interpretation of hot, low-density components in § 6.

5.4. σ Gem

The star σ Gem is a RS CVn–type spectroscopic binary with a K1 III primary and an unseen companion (Engvold et al. 1988). In order to model the stellar emission line better, two observations were taken at different phases, 0.16 and 0.70. This technique was also used on the binary star Capella (Linsky et al. 1995) and HR 1099 (Piskunov et al. 1997). The velocity separation between the stellar and interstellar lines was not more than 60 km s^{-1}, which was not large enough to allow the core of the emission line to be observed. We have no Fe II data for σ Gem, but the Mg II data clearly show two distinct components at 21.6 km s^{-1} and 32.1 km s^{-1}. The velocity separation is 10.5 ± 0.1 km s^{-1}, and the small uncertainty allows us to fix the velocity separation of the D I and H I components when fitting the Lyα region. The fits for the σ Gem Mg II lines are shown in Figures 9 and 10.

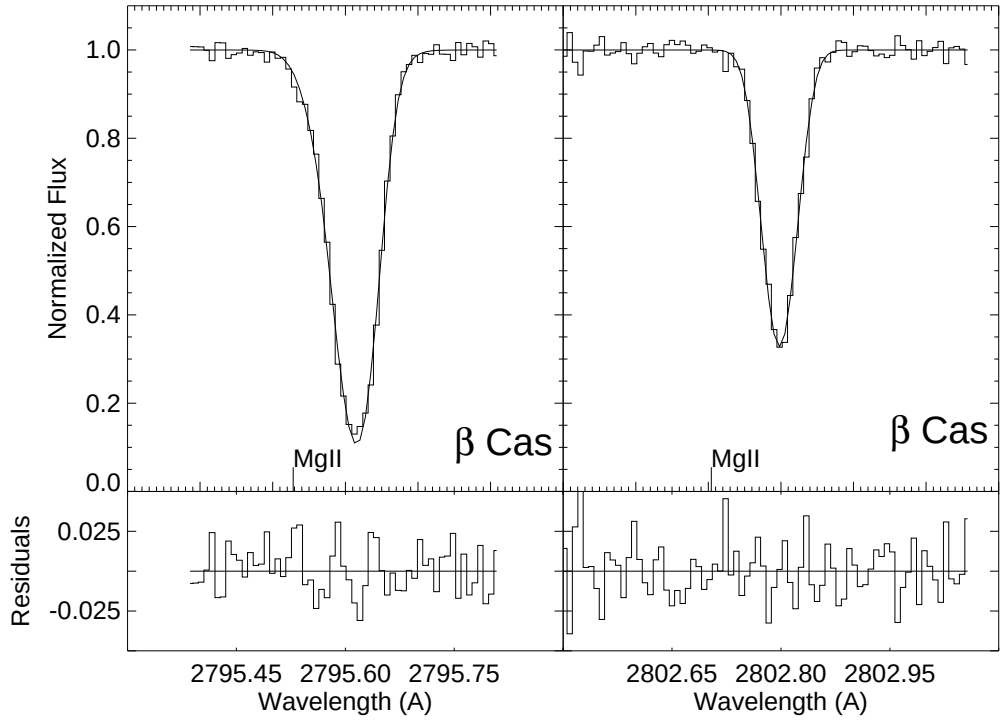

FIG. 2.—Mg II H and K region of β Cas showing the observed spectra, the best-fit model after convolution, and the residuals of the best fit. The continuum is normalized to unity, and the rest wavelengths for Mg II are shown by the labeled tick marks.

The observations at both phases must give the same interstellar absorption parameters. When we fit each spectra separately, we found it very difficult to get agreement between the interstellar parameters due to the two-component degeneracy. We therefore wrote a special routine to fit both spectra with the same interstellar parameters simultaneously, while allowing for different emission line profiles for each spectra. The separation between the two components was held fixed, and since we could not rely on both spectra having the same wavelength calibration, an

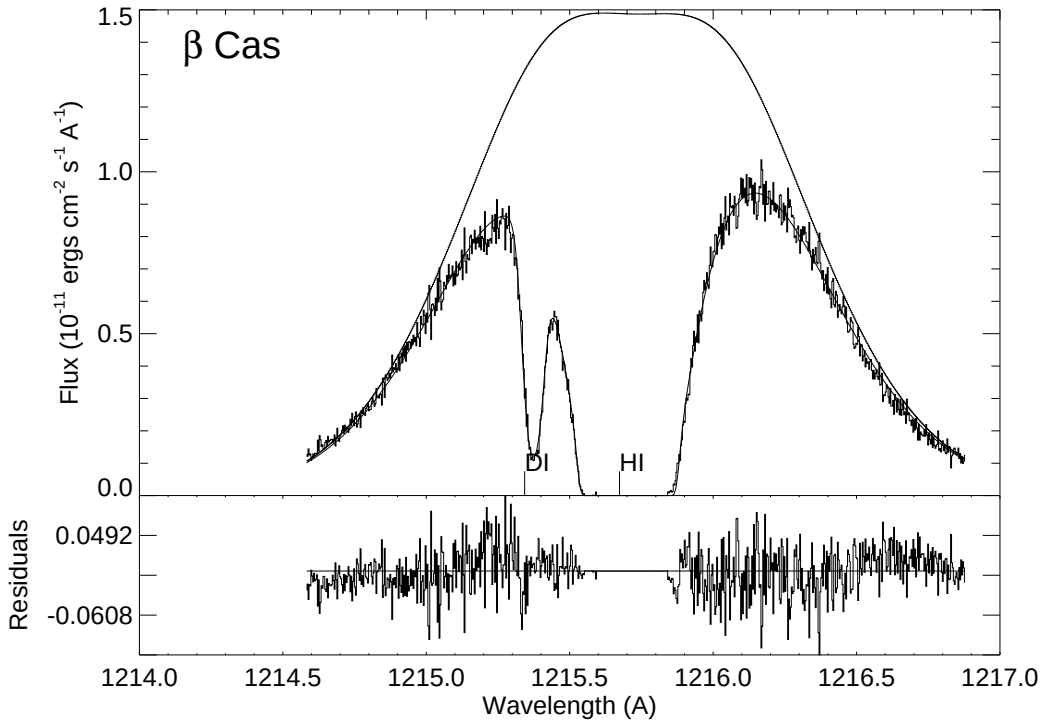

FIG. 3.—Lyα region of β Cas showing the observed spectra, the model stellar emission line, the best-fit model after convolution with the instrumental LSF, and the residuals of the best fit. The rest wavelengths for D I and H I are shown by the labeled tick marks. Only one absorption component is seen toward β Cas.

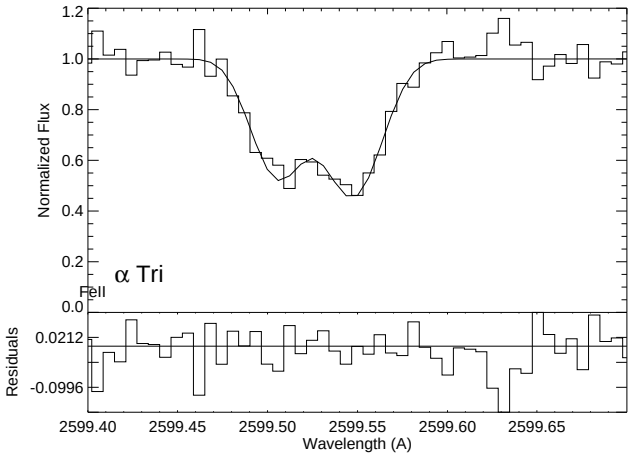

FIG. 4.—Fe II λ2599 region of α Tri showing the observed spectra, the best-fit model ater convolution, and the residuals of the best fit. Two components are seen in the opacity profile. The continuum is normalized to unity, and the rest wavelength for Fe II is shown by the labeled tick mark.

overall wavelength shift was allowed between the interstellar parameters of the two spectra.

The fits for the Lyα region are shown in Figures 11 and 12. Of particular interest are the emission-line profiles for each phase which look quite different. The emission-line profiles for σ Gem actually required three Gaussian components to work since the core region was not Gaussian. The centroid of the part of the emission lines unaffected by interstellar absorption agrees well with the expected velocity of the σ Gem primary, implying that the companion star for σ Gem is unseen at Lyα. We conclude that the Lyα emission for the primary star is variable both in strength and shape. Piskunov et al. (1997) also required different Lyα emission-line profiles for HR 1099 at different orbital phases.

5.5. β Gem

The star β Gem is only 1° away from σ Gem, and so, we might expect that the parameters for the LIC should agree. The Mg II data for β is shown in Figure 13, and the fit parameters do agree very well with the fits from σ Gem. Again, two distinct components can be seen and must therefore be included in the fit for the Lyα region. The velocity separation for the components is 11.1 ± 0.2 km s^{-1}, which is a statistically significant difference from the separation of the components of σ Gem; therefore, when fitting the Lyα region we fixed the component separation at 11.1 km s^{-1}.

In order to produce an acceptable fit we needed to model a very deep self-reversal in the emission line. Because a self-reversal this deep was unexpected, we explored the possibility that there was a stellar hydrogen wall surrounding β Gem. We introduced an emission line with a much shallower self-reversal and added another hot, low-density component to the fit. After finding a new best fit, we found that the test component was both too hot to be interpreted as a stellar hydrogen wall and at the wrong velocity. We therefore rejected the hydrogen wall hypothesis and simply used an emission line with a deep self-reversal. When this emission line was adopted, the fit parameters agreed fairly well with the parameters from σ Gem. The fit for β Gem is shown in Figure 14.

Our fit for β Gem required a column density on average 0.1 dex higher for the second component than did σ Gem in H I, D I, and Mg II. Since β Gem is only 10 pc away and σ

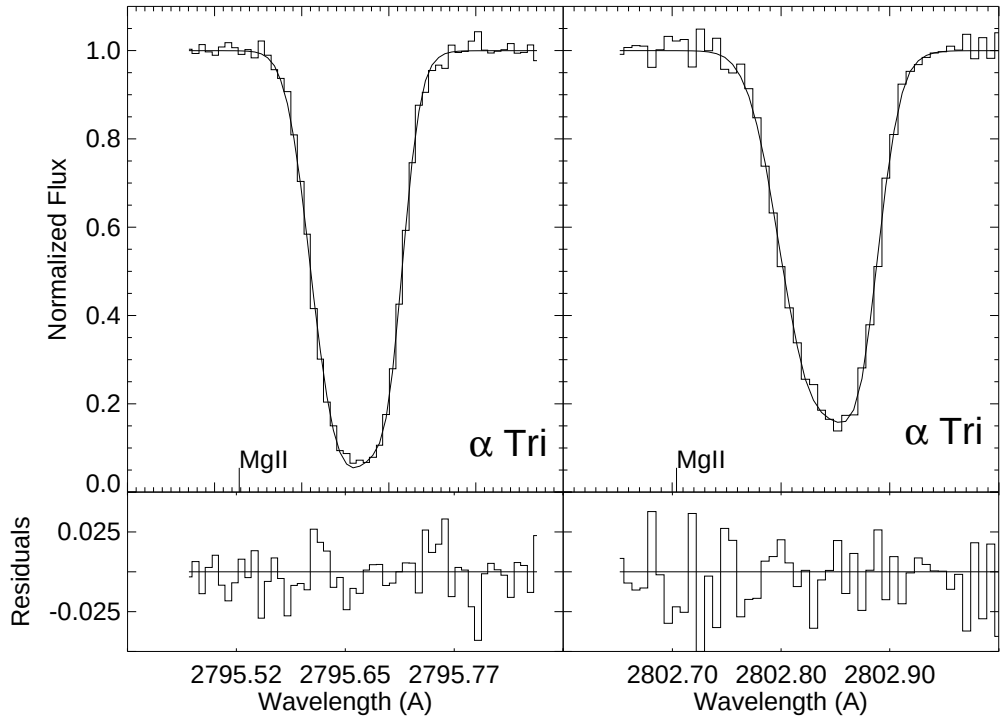

FIG. Fig. 5.—Mg II H and K region of α Tri showing the observed spectra, the best-fit model after convolution, and the residuals of the best fit. Two unresolved components are needed to fit the opacity profiles. The continuum is normalized to unity, and the rest wavelengths for Mg II are shown by the labeled tick marks.

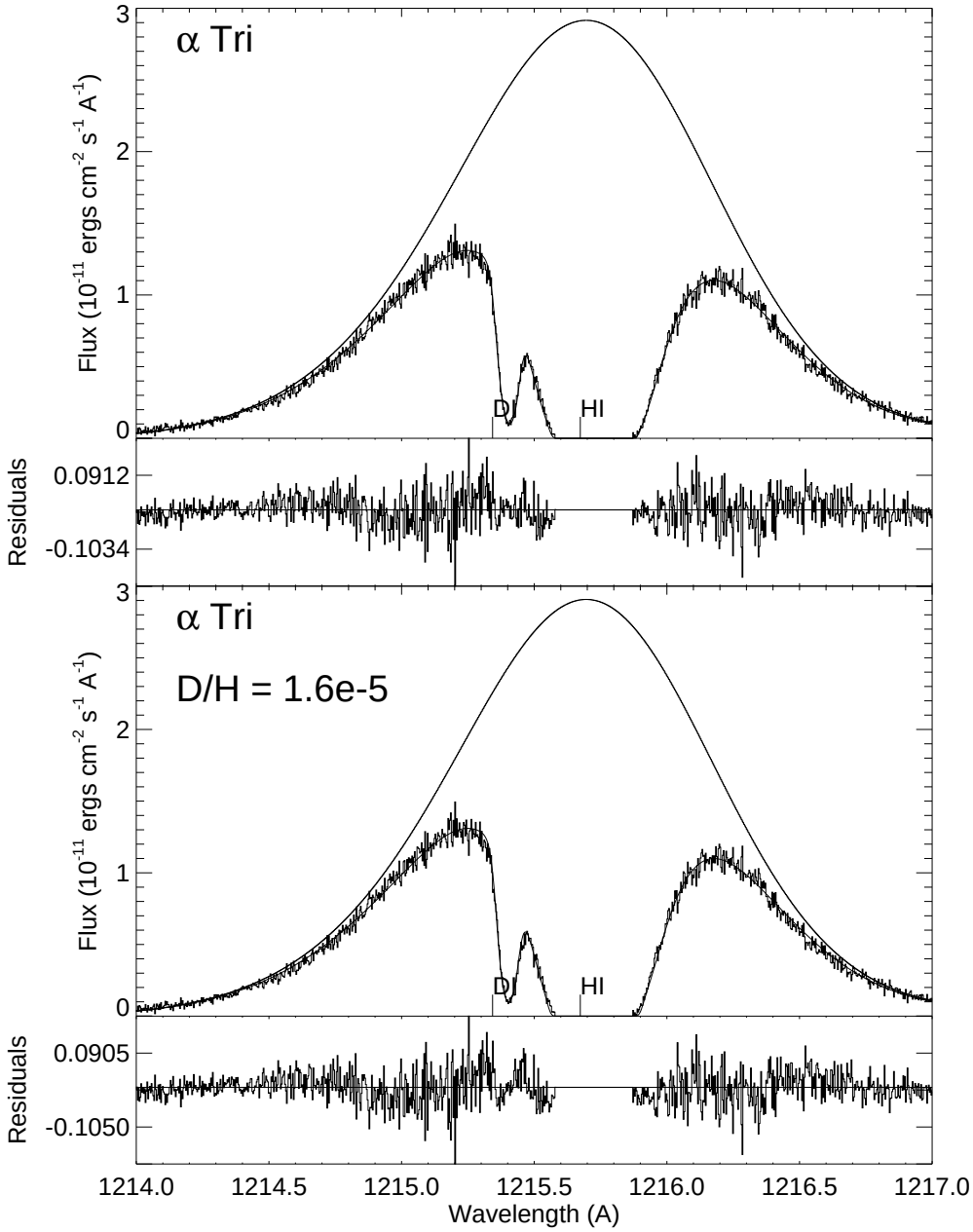

FIG. 6.—Lyα region of α Tri showing the observed spectra, the model stellar emission line, the best-fit model after convolution with the instrumental LSF, and the residuals of the best fit. The rest wavelengths for D I and H I are shown by the labeled tick marks. Two interstellar components are used in the fit. The top plot is the best fit with no constraints on D/H, and the bottom plot shows the best fit with D/H for the LIC component fixed to 1.6×10^{-5}.

Gem is at a distance of 55 pc, this implies that the entire second cloud lies in front of β Gem. The column density changes by 25% on the scale of 1° or 0.17 pc at the distance of β Gem implying clouds, or structures smaller than 1 pc. Clouds smaller than 1 pc have also been seen by Meyer & Blades (1996) and by Dring et al. (1996), although with temperatures below 300 K, these clouds are much colder than the clouds studied in this paper.

5.6. *31 Com*

The Mg II spectra for 31 Com are shown in Figure 15 and are well fitted with only one component. Since these data were taken with the small science aperture (SSA), we used a LSF of width 3.7 pixels, the value given by Gilliland (1994) for the SSA. The Fe II spectrum, shown in Figure 16, is of lower signal to noise but also requires only a single component. The best-fit model for the Lyα region is shown in Figure 17, along with the emission-line profile and the fit residuals. The emission line is very broad, most likely due to the 70 km s^{-1} rotational velocity, and required a broad self-reversal to be included in the emission-line model. Only one absorption feature was needed to produce a good fit, and no additional components were required. Our fit parameters can be compared with the parameters given by Piskunov et al. (1997), who analyzed a lower resolution G140M spectra of the Lyα line of 31 Com. They find $b_{\rm H\,I} = 11.1 \pm 1.3$ and $\log (N_{\rm H\,I}) = 17.95 \pm 0.15$, while we find $b_{\rm H\,I} = 11.96 \pm 0.7$ and $\log (N_{\rm H\,I}) = 17.88 \pm 0.06$ which are consistent within the stated errors. The low value of the H I column density, $\log (N_{\rm H\,I}) = 17.88$, implies the hot, ionized

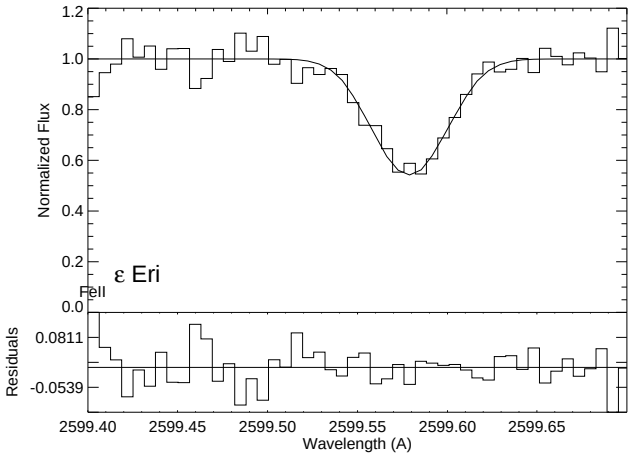

FIG. 7.—Fe II λ2599 region of ϵ Eri showing the observed spectra, the best-fit model after convolution, and the residuals of the best fit. The continuum is normalised to unity, and the rest wavelength for Fe II is shown by the labeled tick mark.

local bubble extends along most of the line of sight toward 31 Com, which lies in the direction of the north galactic pole at a distance of 90 pc.

6. LOW-DENSITY COMPONENTS

In several previous papers the authors needed to include hot, low-density components to fit the H I absorption correctly (Bertin et al. 1995; Gry et al. 1995; Linsky & Wood 1996; Wood, Alexander & Linsky 1996), and these components have been interpreted either as hydrogen walls formed in the heliopause (or astropause) or as gas evaporating from the LIC at the HISM interface. Both interpretations require specific properties to be observed of the absorption component for them to work. Hydrogen walls are difficult to see in the downwind direction of the heliopause, so we expect they will be important only for stars in the upwind direction. In the case of stellar hydrogen walls, the star must lie inside a warm cloud and not the ionized HISM. Further, the line of sight velocity of the absorption must match the predicted velocity of the hydrogen wall, which generally lies between the star's radial velocity and the radial velocity of the relevant cloud. Finally, any constraints which can be placed on the line width must be consistent with the expected temperature of the hydrogen wall, which is a function of relative star/cloud velocity.

For the LIC interface interpretation, we do not expect to see additional absorption along lines of sight that do not pass through the interface, but we do reasonably expect that a significant fraction of the lines of sight which pass through the interface should show additional absorption. The line velocity should be redshifted with respect to the LIC velocity, or at worst at the same velocity as the LIC, consistent with material moving out of the cloud. It would be difficult for this model to explain a significant blueshift. Also, evaporation models predict absorption from higher ionization species as C IV, Si IV, and N V, although these predictions vary according to the model.

In fitting the H I absorption, we took the position that if a hot, low-density component was not needed, it should not be included in the fit. We were able to obtain high-quality fits for all the data except ϵ Eri, which did require an additional low-density component. This fact actually supports the hydrogen wall hypothesis since detection of a solar hydrogen wall is only practical along the line of sight toward 31 Com, and most of our stars lie at distances greater than 10 pc, placing them in the HISM where stellar hydrogen walls should not be found. The distance of ϵ Eri

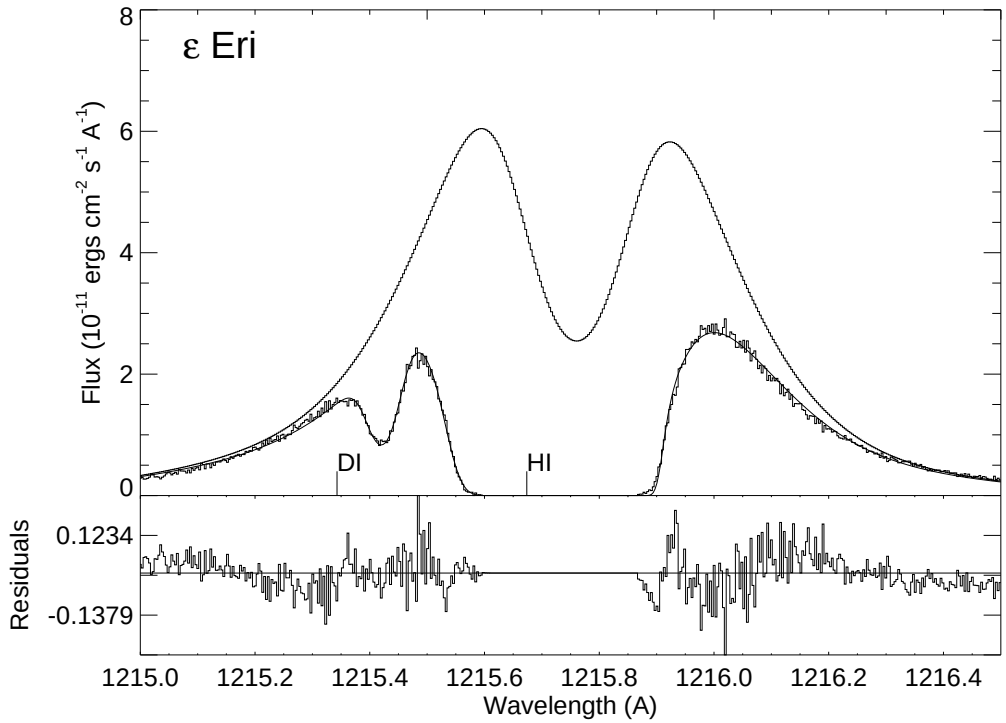

FIG. 8.—Lyα region of ϵ Eri showing the observed spectra, the model stellar emission line, the best-fit model after convolution with the instrumental LSF, and the residuals of the best fit. The rest wavelengths for D I and H I are shown by the labeled tick marks. An additional hot, low-density component was needed to produce the fit shown.

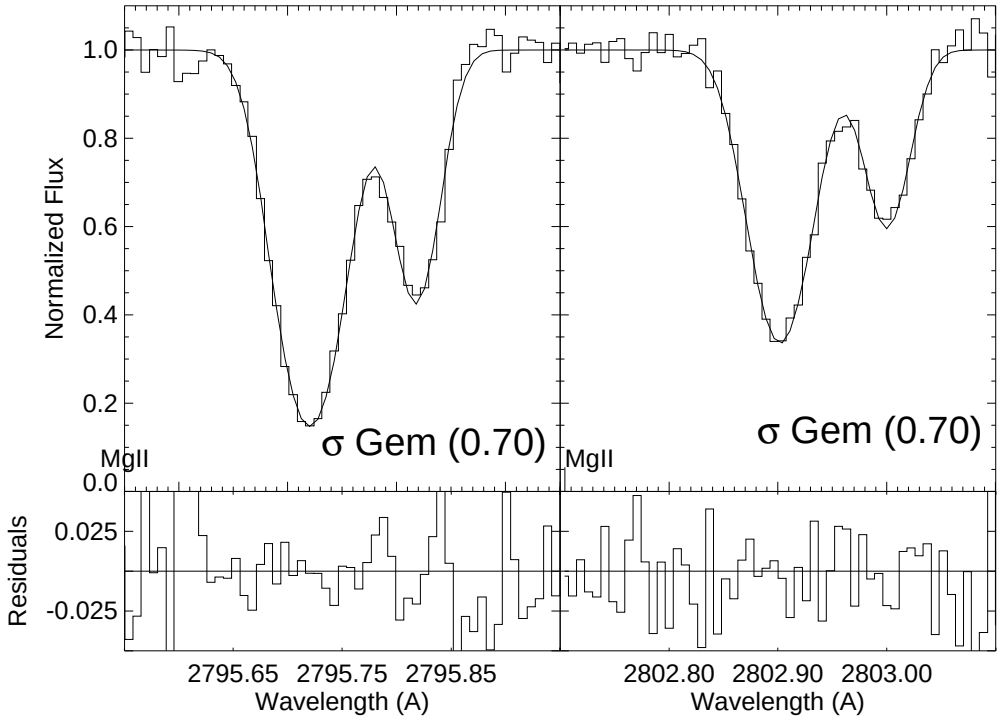

FIG. 9.—Mg II H and K region of σ Gem, orbital phase 0.697, showing the observed spectra, the best-fit model after convolution, and the residuals of the best fit. The continuum is normalized to unity, and the rest wavelengths for Mg II are shown by the labeled tick marks. Two components are easily resolved in the spectra.

(3.3 pc) places it outside the LIC edge (2.4 pc assuming a constant space density of 0.1 H cm^{-3}) but could easily be located inside the LIC if the density is not constant. Therefore, ϵ Eri is the only star for which a stellar hydrogen wall is expected, and it is the only star which actually requires a hot, low-density component. The evaporative interface model predicts just the reverse; since every line of sight, with the possible exception of ϵ Eri, passes through the LIC

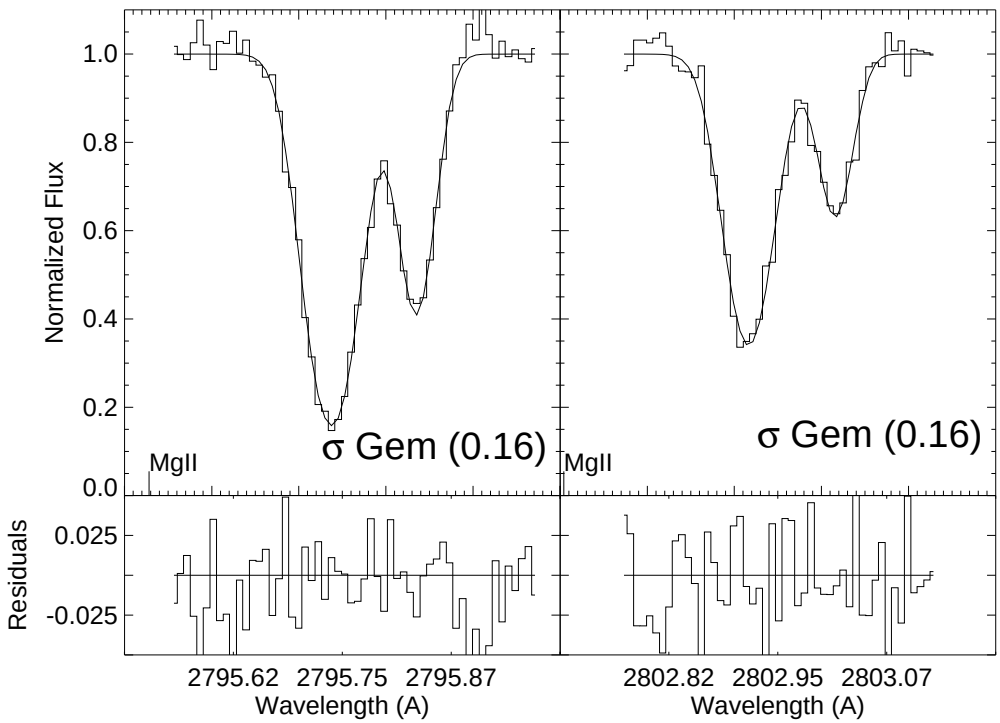

FIG. 10.—Mg II H and K region of σ Gem, orbital phase 0.158, showing the observed spectra, the besf-fit model after convolution, and the residuals of the best fit. The continuum is normalized to unity, and the rest wavelengths for Mg II are shown by the labeled tick marks. Two components are easily resolved in the spectra.

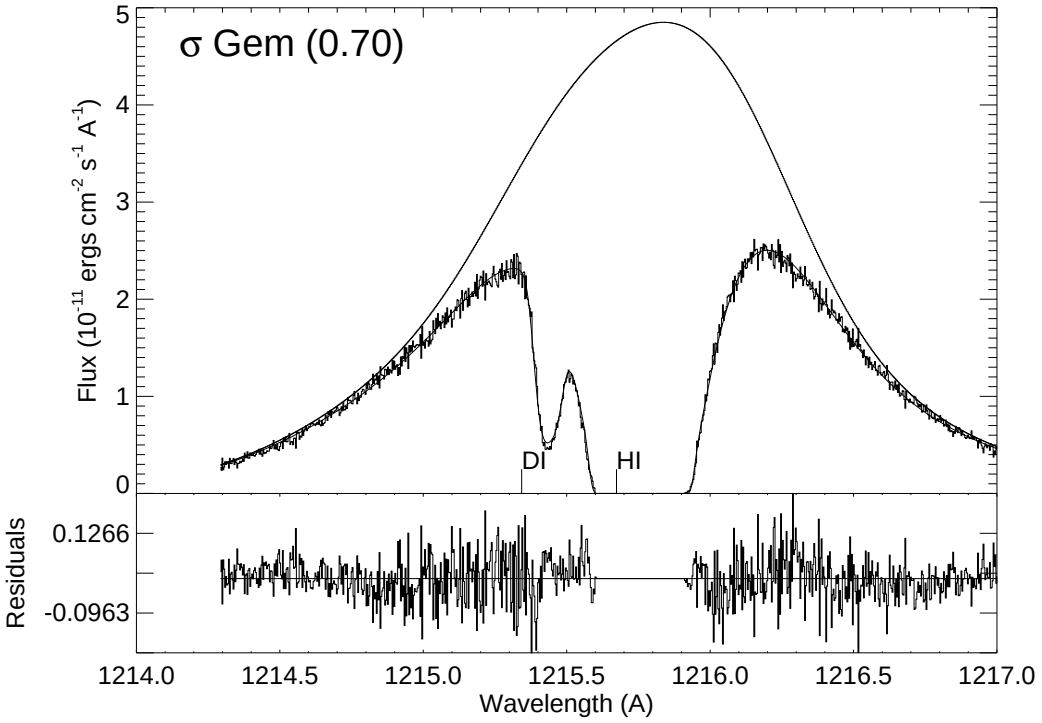

FIG. 11.—Lyα region of σ Gem, orbital phase 0.697, showing the observed spectra, the model stellar emission line, the best-fit model after convolution with the instrumental LSF, and the residuals of the best fit. The rest wavelengths for D I and H I are shown by the labeled tick marks. Both the fit for phases 0.697 and for phase 0.158 use the same interstellar parameters.

interface, we would have expected more of the stars to require a low-density component. It is not clear that the interface model requires an extra component along every line of sight which passes through the interface, nor can we rule out with certainty that the five lines of sight which pass through the interface have a hot, low-density component, but the observed distribution of hot, low-density components favors the hydrogen wall hypothesis.

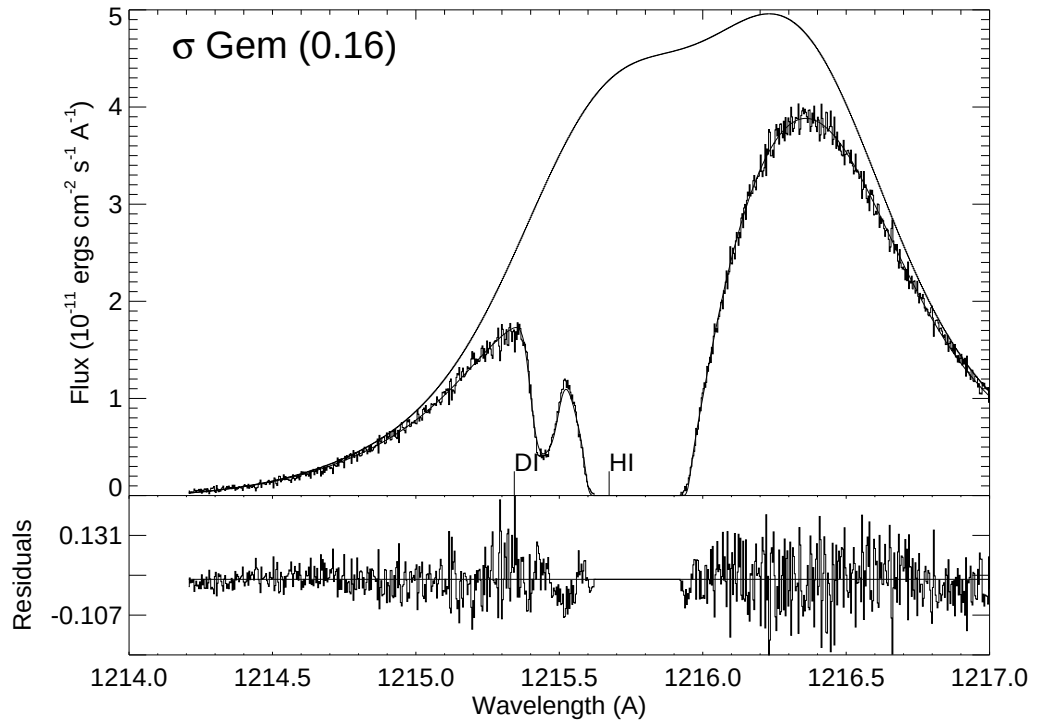

FIG. 12.—Lyα region of σ Gem, orbital phase 0.158, showing the observed spectra, the model stellar emission line, the best-fit model after convolution with the instrumental LSF, and the residuals of the best fit. The rest wavelengths for D I and H I are shown by the labeled tick marks. Both the fit for phase 0.697 and for phase 0.158 use the same interstellar parameters.

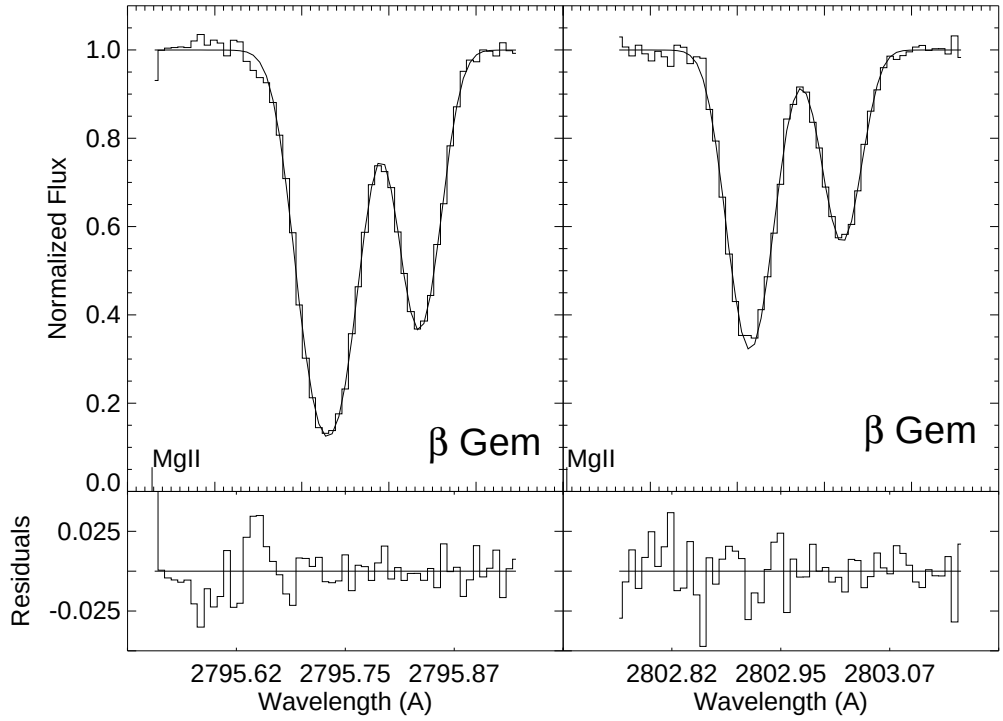

FIG. 13.—Mg II H and K region of β Gem showing the observed spectra, the best-fit model after convolution, and the residuals of the best fit. The continuum is normalized to unity, and the rest wavelengths for Mg II are shown by the labeled tick marks. Two components are easily resolved in the spectra.

The direction of ϵ Eri lies 148° from the upwind direction of the LIC velocity vector, and since the hydrogen walls are difficult to detect in the downward direction, it is extremely unlikely that the extra component can be associated with a solar hydrogen wall. To investigate the stellar hydrogen wall hypothesis, we needed to determine the velocity of ϵ Eri through its local cloud and the angle between its upwind direction and our line of sight. The star lies only 3.3 pc away, and the velocity of the best-fit D I and H I lines (with hot component included) agrees with the projected LIC

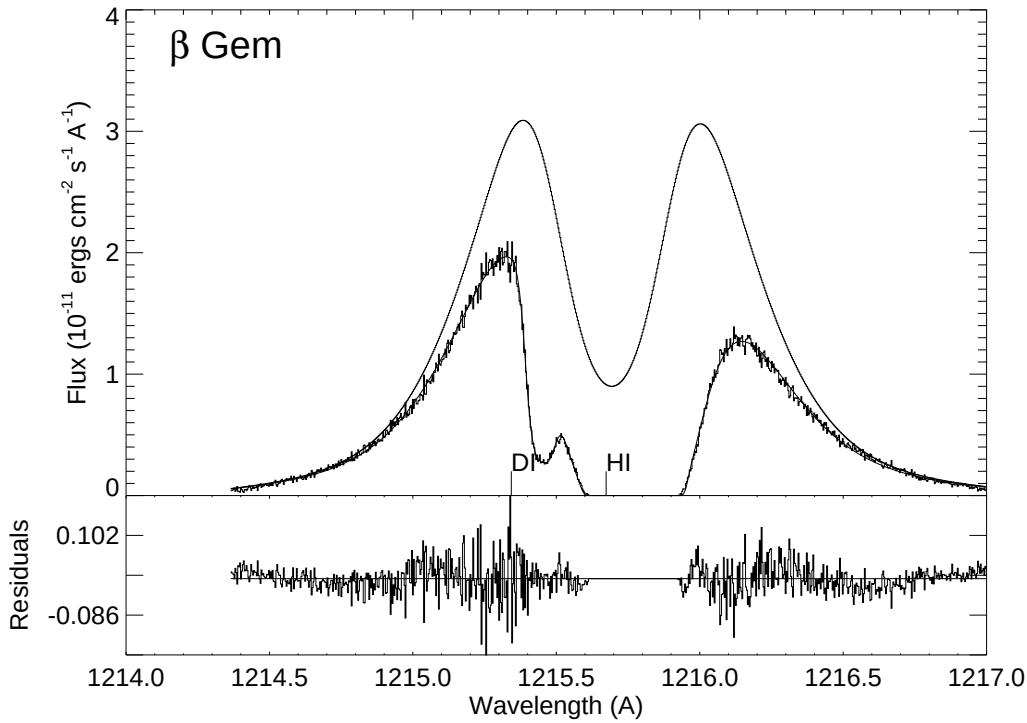

FIG. 14.—Lyα region of β Gem showing the observed spectra, the model stellar emission line, the best-fit model after convolution with the instrumental LSF, and the residuals of the best fit. The rest wavelengths for D I and H I are shown by the labeled tick marks. The model parameters agree well with the fits from σ Gem.

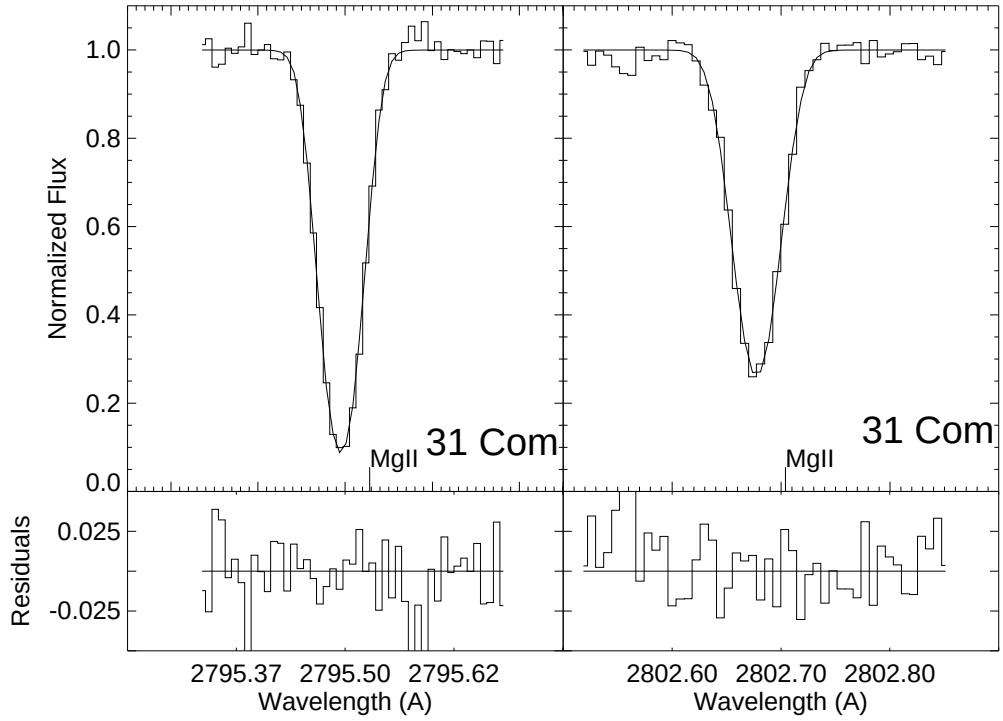

FIG. 15.—Fe II λ2599 region of 31 Com showing the observed spectra, the best-fit model after convolution, and the residuals of the best fit. The continuum is normalized to unity, and the rest wavelength for Fe II is shown by the labeled tick mark.

velocity. We have assumed that ϵ Eri is embedded in the LIC, making a hydrogen wall possible; however, the space density inferred from the measured column density is 0.076 H cm^{-3}, which is lower than the typical space density of 0.10–0.16 H cm^{-3} associated with the LIC (Linsky et al. 1997). The stellar hydrogen wall hypothesis may then require a clumpy LIC to fit the data. The next step was to determine the relative velocity of ϵ Eri and the LIC. We obtained radial velocity and proper motions from the Simbad database, which are listed in Table 5, and computed a relative velocity of 27.3 km s^{-1} in the direction of $l = 207\overset{\circ}{.}8$ and $b = 19\overset{\circ}{.}7$. Our line of sight was then only 69° from the upwind direction of ϵ Eri, consistent with the stellar hydrogen wall hypothesis.

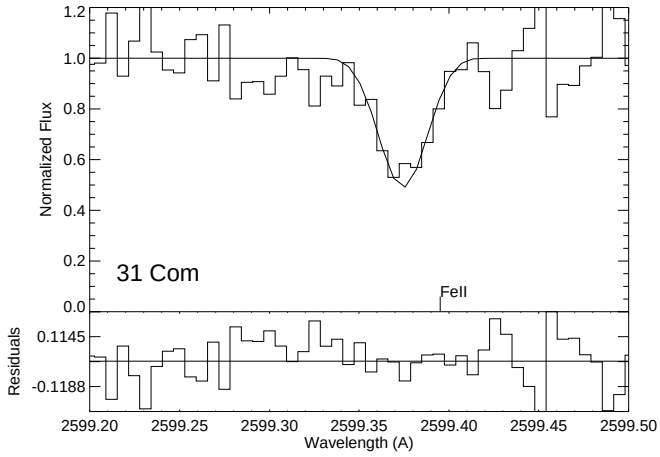

FIG. 16.—Mg II H and K region of 31 Com showing the observed spectra, the best-fit model after convolution, and the residuals of the best fit. The continuum is normalized to unity, and the rest wavelengths for Mg II are shown by the labeled tick marks.

It remained only to compute the expected velocity of the hot component. In general, the interstellar material is slowed down on entering the astropause, and the expected velocity should lie between the star's radial velocity and the projected velocity of the LIC. For ϵ Eri the radial velocity was +16 km s^{-1}, and the projected LIC velocity was +21.6 km s^{-1}. The velocity of the hot component was very uncertain, however, since it could be redshifted and broadened, yet still yield a good fit. The combination of $b_{\rm H\,I}$ and v_c parameters ranged from $b = 19.5$ km s^{-1} and $v_c = 2.3$ km s^{-1} to $b = 23.3$ km s^{-1} and $v_c = 15$ km s^{-1}, the latter being acceptable for a stellar hydrogen wall. The hot component is clearly blueshifted with respect to the LIC by at least 6 km s^{-1}, making the interface hypothesis unlikely. Overall, the stellar hydrogen wall interpretation works best.

7. DISCUSSION

It is useful to discuss the observational results in terms of a model that can provide a framework for interpretation. We tentatively construct a model of a warm, $T = 7000$–

TABLE 5

PARAMETERS FOR COMPUTING INTERSTELLAR WIND VELOCITIES

Star	Distance (pc)	v_r (km s^{-1})	μ_α (arcsec yr^{-1})	μ_δ (arcsec yr^{-1})	v_0 (km s^{-1})	l (deg)	b (deg)	θ (deg)
ϵ Eri.....	3.3	16.0	−0.975	0.22	27.3	207.8	19.7	68

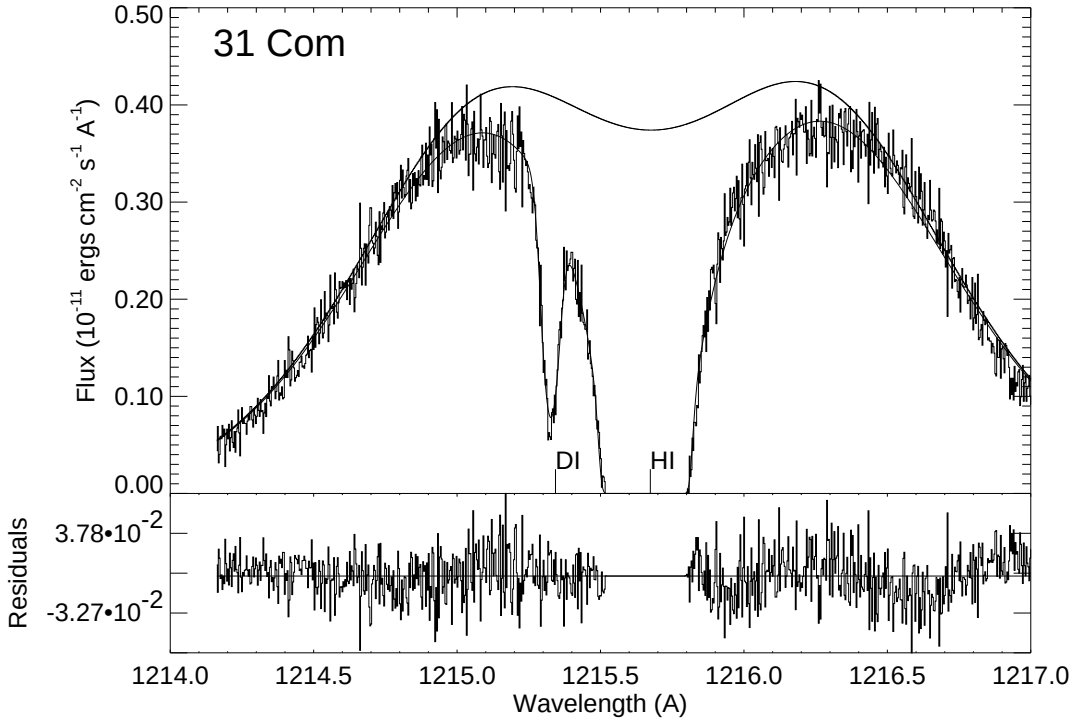

FIG. 17.—Lyα region of 31 Com showing the observed spectra, the model stellar emission line, the best-fit model after convolution with the instrumental LSF, and the residuals of the best fit. The rest wavelengths for D I and H I are shown by the labeled tick marks. Only one component is needed to fit the interstellar absorption.

9000 K, partially ionized cloud enveloping the solar system and extending for several parsecs in some directions. We refer to this cloud as the LIC and identify it as the AG cloud of Lallement et al. (1995). The LIC is surrounded by several small clouds which are distinguished by their radial velocities. Surrounding this group of clouds is the hot, ionized, local bubble which is not seen in absorption.

Given this model every star should exhibit a velocity component at the projected line of sight velocity of the LIC. The stars β Cas, α Tri, and ϵ Eri all have components with velocities within 1 km s^{-1} of the projected LIC velocity. For β Gem and σ Gem the closest velocity to the projected LIC velocity is redshifted by about 2 km s^{-1}. This shift is close to the estimated systematic uncertainty, so these components are marginally consistent with the LIC velocity but the discrepancy is large. For 31 Com the single component found is redshifted with respect to the projected LIC velocity by about 4 km s^{-1} and is not consistent with the LIC velocity. Piskunov et al. (1997) also find a redshifted component along the line of sight to 31 Com, which is toward the north galactic pole, and pointed out that the original sample used by Lallemont et al. (1995) did not contain any stars at high Galactic latitude. Ca II absorption, looked at by Vallegra et al. (1993), shows several stars with $b > 60°$ including η UMa and α CVn with velocities redshifted by 3–4 km s^{-1} with respect to the projected LIC velocity. It seems therefore that toward the North Galactic Pole there is either a separate cloud moving at a slightly different velocity or that the LIC is moving in a nonrigid manner. The former would by supported by observations at more intermediate latitudes showing both velocity components, while the latter would be supported by intermediate latitudes exhibiting single components with velocities midway between the LIC and 31 Com.

We interpret the second components toward β Gem, σ Gem, and α Tri to be distinct clouds since both the LIC velocity and the second component are visible in the same line of sight. The second component for α Tri is unresolved and blueshifted with respect to the LIC velocity, implying that the cloud is moving toward the LIC. The second component for the pair of Gemini stars is clearly resolved in the Mg II data and has essentially the same column density for each star. The second cloud must therefore lie in front of β Gem, within a distance of 10 pc, and must have a relatively small extent.

7.1. *D/H Ratio*

Our best D/H measurement is in the direction of β Cas, with D/H = $1.7 \pm 0.3 \times 10^{-5}$, consistent with the value of D/H = $1.6 \pm 0.2 \times 10^{-5}$ found by Linsky et al. (1995) and with the value of D/H = 1.6×10^{-5} found by Landsman, Sofia, & Bergeron (1996) toward HZ 43. Despite the high quality of the data, it is not possible to determine if there are deviations in the D/H ratio due to the large uncertainties in the H I column density caused by uncertaint stellar emission lines and possible unaccounted for components. Although the D/H values of the other lines of sight vary, they all agree with a value of 1.6×10^{-5} within their error bars. Specifically, for each case we were able to fix the D/H ratio for the LIC at 1.6×10^{-5} and obtain an acceptable fit to the data. For the second components along the line of sight toward α Tri and the β Gem, we obtained a best fit with a lower D/H ratio. Lemoine et al. (1996) also find a lower D/H ratio in clouds outside the LIC toward the star G191-B2B. While D/H seems to be constant in the LIC, it may yet vary in other clouds. Given the typical uncertainties in measuring

D/H, this may only be verified when a large number of observations through another cloud are available or when the FUSE mission is launched.

7.2. *Gas Depletions*

The gas phase depletions for Mg II and Fe II are defined by $D(\mathrm{Mg}) = \log(\mathrm{Mg/H\ I}) - \log(\mathrm{mg/H\ I})_{\odot}$, and $D(\mathrm{Fe}) = \log(\mathrm{Fe\ II/H\ I}) - \log(\mathrm{Fe/H})_{\odot}$. The solar values, according to Anders & Grevesse (1989), are $\log(\mathrm{Mg/H})_{\odot} = -4.41$ and $\log(\mathrm{Fe/H})_{\odot} = -4.49$. The depletions for our lines of sight are listed in Table 3, and range from -0.8 to -1.44 for Mg II and -0.8 to -1.3 for Fe II. These should be compared with the values from Piskunov et al. (1997) who find that $D(\mathrm{Mg\ II}) = -1.1 \pm 0.2$ for the LIC. These depletion values assume no H I ionization in the LIC and thus overestimate the depletion. The ionization fraction for H I has been measured (Vennes et al. 1993; Lallement et al. 1994; Frisch 1994; Holberg et al. 1995; Dupuis et al. 1995; Lanz et al. 1996; Barstow et al. 1996; Wood & Linsky 1997) with values of $X(\mathrm{H}) \equiv n(\mathrm{H\ II})/[n(\mathrm{H\ I}) + n(\mathrm{H\ II})]$ ranging from 0.35–0.7. If we assume Mg is mostly in Mg II then the depletions are overestimated by $\log[1 - \mathrm{X}(H)] = 0.19$–0.52 dex. Despite this, the depletion values show large variability along different lines of sight and must change significantly over just a few parsecs in the LISM.

Given the three species H I D I and Mg II we can compute three ratio parameters D/H, D(Mg), and D/Mg II. Both the D(Mg) and the D/Mg II parameters vary considerably more than the D/H ratio, which can be understood in two ways. Some regions of the LISM could have been recently shocked, destroying grains and producing larger abundances of Mg II. Alternatively the variability could be due to real variations in the H ionization fraction. Since D I and H I must share the same ionization properties, it is not surprising that D/H is relatively more constant than $D(\mathrm{Mg})$ or D/Mg II. It is clear that deuterium is a better tracer of hydrogen then Mg II in the LISM.

7.3. *Temperature and ξ Values*

The temperatures and microturbulence, ξ, values for each of the clouds are listed in Table 3. Our temperatures fall in the range 7800–9700 K for the LIC and in the range 7000–8300 K for the other cloud components. Our temperatures are higher than the 7000 ± 900 K found by Linsky et al. (1995) for the LIC along the line of sight to Capella. To ensure that there was no error in the processing we analyzed the archival spectra of Capella using the same techniques described here and found a temperature of 7200 K, consistent with the value of Linsky et al. (1995). Despite the good agreement there may still be systematic errors in our results if there are additional components with smaller column densities and higher temperatures. Since our fits are generally very good, adding additional hotter components would not produce any improvement and would only make the column density measurement more uncertain. There is also no good reason to assume that the temperature is the same for different lines of sight, so our temperature variations may in fact be real.

8. CONCLUSIONS

The value of D/H in the LIC for all our lines of sight is consistent with the value 1.6×10^{-5} found by Linsky et al. (1995). We cannot say with certainty that there is no variation in the D/H ratio due mainly to large uncertainties in the measured values of the saturated H I line. Measuring the H I line is complicated by the unknown Lyα emission lines and by the possible presence of multiple, unresolved absorption features. Despite these problems, analyses of the lines of sight toward β Cas and 31 Com in this paper, and Piskunov et al. (1997), using two different techniques, obtain results that are in good agreement with each other. It was also found that deuterium is a better tracer of hydrogen than Mg II for the LISM.

For every line of sight, we investigated the possibility that there was a hot additional component in the absorption but found it necessary to include such a component only in the case of ϵ Eri. We considered both the possibility that this could be a stellar hydrogen wall or that it could be a hotter region evaporating off the LIC/HISM interface. We concluded that since the star most likely lies inside the LIC and since the hot component was blueshifted with respect to the LIC that it could not be an interface phenomena but was most likely a stellar hydrogen wall. Despite this, we cannot rule out the possibility that interface phenomenon may be important.

We found absorption at the LIC projected velocity along three lines of sight, two lines of sight having a velocity marginally consistent with the LIC. However, 31 Com exhibited a velocity which differed from the accepted LIC velocity by about 4 km s^{-1}. This may mean that the LIC is not a rigid body or that thee is a separate cloud in the direction of the North Galactic Pole. We also observed extra components along three lines of sight which are perhaps best explained as cloudlets, smaller than about 1 pc, moving roughly with the LIC but with small velocity differences. Finally, the lack of extra components toward stars like 31 Com, at a distance of 90 pc, implies that the Local Bubble extends for large distances in certain directions.

We would like to thank Brian Wood for his helpful comments and suggestions. This research has made use of the Simbad database, operated at CDS, Strasbourg, France. J. L. is supported by STScI grant GO-05879.02-94A to the University of Colorado.

REFERENCES

Anders, E., & Grevesse, N. 1989, Geochim. Cosmochim. Acta, 53, 197
Balsiger, H., Altwegg, K., & Geiss, J. 1995, J. Geophys. Res., 100, 5827
Boato, G. 1954a, Geochim. Cosmochim. Acta, 6, 209
———. 1954b, Geochim. Cosmochim. Acta, 36, 347
Baranov, V. B., & Malama, Y. G. 1995, J. Geophys. Res., 100, 14755
Barstow, M. A., Dobbie, P. D., Holberg, J. B., Hubeny, I., & Lanz, T. 1997, MNRAS, 286, 58
Bertin, P., Vidal-Madjar, A., Lallement, R., Ferlet, R., & Lemoine, M. 1995, A&A, 302, 889
Bevington, P. R. 1969, Data Reduction and Error Analysis for the Physical Sciences (New York: McGraw-Hill)
Borkowski, K. J., Balbus, S. A., & Fristrom, C. C. 1990, ApJ, 355, 501
Brekke, P., Kjeldseth-Moe, O., Bartoe, J.-D. F., & Brueckner, G. E. 1991, ApJS, 75, 1337
Carswell, R. F., et al. 1996, MNRAS, 278, 506
Cox, D. P., & Reynolds, R. J. 1987, ARA&A, 25, 303
Dalton, W. W., & Balbus, S. A. 1993, ApJ, 404, 625
Dring, A. R., Murthy, J., Henry, R. C., & Walker, H. J. 1996, ApJ, 457, 764
Dupuis, J., Vennes, S., Bowyer, S., Pradhan, A. K., & Thejll, P. 1995, ApJ, 455, 574
Eker, Z. 1985, Wisconsin Astrophys. No. 226, Washburn Obs. (Madison, WI: Univ. Wisconsin Press)
Engvold, O., et al. 1988, A&A, 192, 234
Epstein, R. I., Lattimer, J. M., & Schramm, D. N. 1976, Nature, 263, 198

Frisch, P. C. 1994, Science, 265, 1423
Frisch, P. C., & York, D. G. 1983, ApJ, 271, L59
Gautier, D., & Owens, T. 1989, in Origin and Evolution of Planetary and Satellite Atmospheres, ed. S. K. Atreya et al. (Tucson: Univ. Arizona Press), 487
Geiss, J., & Reeves, H. 1981, A&A, 93, 189
Gilliland, R. L. 1994, Line Spread Functions and Resolution for GHRS-LSA Spectra with COSTAR, GHRS Instum. Sci. Rep. 063 (Baltimore, MD: STScI)
Gry, C., Lemonon, L., Vidal-Madjar, A., Lemoine, M., & Ferlet, R. 1995, A&A, 302, 497
Holberg, J. B., Barstow, M. A., Bruhweiler, F. C., & Sion, E. M. 1995, ApJ, 453, 313
Lallement, R., & Bertin, P. 1992, A&A, 266, 479
Lallement, R., Bertin, P., Ferlet, R., Vidal-Madjar, A., & Bertaux, J. C. 1994, A&A, 286, 898
Lallement, R., Ferlet, R., Lagrange, A. M., Lemoine, M., & Vidal-Madjar, A. 1995, A&A, 304, 461
Lampton, M., Margon, B., & Bowyer, S. 1976, ApJ, 208, 177
Landsman, W., Sofia, U. J., & Bergeron, P. 1996, Science with the Hubble Space Telescope, Vol. 2 (Baltimore, MD: STScI), 454
Lanz, T., Barstow, M. A., Hubeny, I., & Holberg, J. B. 1996, ApJ, 473, 1089
Lemoine, M., Vidal-Madjar, A., Bertin, P., Ferlet, R., Gry, C., & Lallement, M. 1996, A&A, 308, 601
Linsky, J. L., Diplas, A., Wood, B. E., Brown, A., Ayres, T. R., & Savage, B. D. 1995, ApJ, 451, 335
Linsky, J. L., Piskunov, N., & Wood, B. E. 1996, BAAS, 28, 892
Linsky, J. L., & Wood, B. E. 1996, ApJ, 463, 254
Meyers, D. M., & Blades, J. C. 1996, ApJ, 464, L179
Morton, D. C. 1991, ApJS, 77, 119
Piskunov, N., Wood, B. E., Linsky, J. L., Dempsey, R. C., & Ayres, T. R. 1997, ApJ, 474, 315
Rugers, M., & Hogan, C. J. 1996, ApJ, 459, L1
Schramm, D. N. 1993, in Origin and Evolution of the Elements, ed. N. Prantzos, E. Vangioni-Flam, & M. Cassé (Cambridge: Cambridge Univ. Press), 112
Soderblom, D. R., Gonnella, A., Hulbert, S. J., Leitherer, C., Schultz, A., & Sherbert, L. E. 1993, HST Goddard High Resolution Spectrograph Instrument Handbook, Version 6.0 (Baltimore, MD: STScI)
Songaila, A., Wampler, E. J., & Cowie, L. L. 1997, Nature, 385, 137
Spitzer, L., Jr., & Fitzpatrick, E. L. 1993, ApJ, 409, 299
Tytler, D., Fan, X.-M., & Burles, S. 1996, Nature, 381, 207
Vallerga, J. V., Vedder, P. E., Craig, N., & Welsh, B. Y. 1993, ApJ, 411, 729
Vennes, S., Dupuis, J., Rumph, T., Drake, J., Bowyer, S., Chayer, P., & Fontaine, G. 1993, ApJ, 410, L119
Welsh, B. Y. 1991, ApJ, 373, 556
Welsh, B. Y., Craig, N., Vedder, P. W., & Vallerga, J. V. 1994, ApJ, 437, 638
Wood, B. E., Alexander, W. R., & Linsky, J. L. 1996, ApJ, 470, 1157
Wood, B. E., & Linsky, J. L. 1997, ApJ, 474, L39